# A computationally designed fluorescent biosensor for D-serine

Vanessa Vongsouthi[1†], Jason H. Whitfield[1†], Petr Unichenko[2], Joshua A. Mitchell[1], Björn Breithausen[2], Olga Khersonsky[3], Leon Kremers[2], Harald Janovjak[4], Hiromu Monai[5], Hajime Hirase[5], Sarel J. Fleishman[3], Christian Henneberger[2,6,7], Colin J. Jackson[1*]

[1]Research School of Chemistry, Australian National University, Canberra, Australia
[2]Institute of Cellular Neurosciences, Medical Faculty, University of Bonn, Bonn, Germany
[3]Department of Biomolecular Sciences, Weizmann Institute of Science, Rehovot, Israel
[4]Australian Regenerative Medicine Institute (ARMI), Faculty of Medicine, Nursing and Health Sciences, Monash University, Clayton/Melbourne, Australia
[5]Laboratory for Neuron-Glia Circuitry, RIKEN Center for Brain Science, Wako, Japan
[6]Institute of Neurology, University College London, London, United Kingdom
[7]German Center for Degenerative Diseases (DZNE), Bonn, Germany

[†]These authors contributed equally.
[*]Corresponding authors.

## Abstract

Periplasmic solute-binding proteins (SBPs) have evolved to balance the demands of ligand affinity, thermostability and conformational change to carry out diverse functions in small molecule transport, sensing and chemotaxis. Although the ligand-induced conformational changes that occur in SBPs make them useful components in biosensors, their complexity can be difficult to emulate and they are challenging targets for protein engineering and design. Here we have engineered a fluorescent biosensor with specificity for the signalling molecule D-serine (D-SerFS) from a D-alanine-specific SBP. Through a combination of binding site and remote mutations, the affinity, specificity and thermostability were optimized to allow the detection of changes in D-serine levels using two-photon excitation fluorescence microscopy *in situ* and *in vivo*. This work illustrates the multidimensional constraints that are imposed by the trade-offs between structural dynamics, ligand affinity and thermostability, and how these must be balanced to achieve desirable activities in the engineering of complex, dynamic proteins.

## Introduction

D-amino acids have been discovered in a range of biological organisms (Corrigan, 1969). Free D-serine, in particular, was first found in mammalian brain tissue in the early 1990s using gas chromatography-mass spectrometry (GC-MS) (Hashimoto et al., 1992). Since then, there has been considerable interest in the physiological and pathophysiological role of this molecule. It is now well known that D-serine acts as a co-agonist of excitatory glutamate receptors of the N-methyl-D-

aspartate receptor (NMDAR) subtype. Together with the primary agonist, L-glutamate, D-serine binds to the 'glycine-binding site' on the NR1 binding domain of the NMDAR to activate it (Mothet et al., 2000; Panatier et al., 2006; Schell, Molliver, & Snyder, 1995). By the same mechanism, glycine also acts as a co-agonist of the NMDARs (Mothet et al., 2000; Panatier et al., 2006; Schell et al., 1995). Previous work has demonstrated the preferential gating of synaptic NMDARs by D-serine (Henneberger, Papouin, Oliet, & Rusakov, 2010; T. Papouin et al., 2012), and of extrasynaptic NMDARs by glycine (T. Papouin et al., 2012). Notably, it is synaptic NMDARs that are primarily responsible for inducing long-term potentiation (LTP) of excitatory synaptic transmission, a key mechanism of learning and memory (T. V. Bliss & Collingridge, 1993; T. V. P. Bliss & Cooke, 2011; Hardingham & Bading, 2010).

D-serine has been associated with a number of conditions centred on cognitive impairment and disturbances to NMDAR activity. D-serine levels in the brain are largely regulated by the activity of serine racemase (SR), which racemizes L-serine to produce D-serine, and D-amino acid oxidase (DAAO), which catabolises it (Pollegioni & Sacchi, 2010; H. Wolosker, Blackshaw, & Snyder, 1999). Abnormal levels of both SR and DAAO have been associated with schizophrenia and Alzheimer's disease (Basu et al., 2009; Labrie et al., 2009; Madeira et al., 2015). Recent studies in flies and mammals have also implicated D-serine in sleep regulation (Dai et al., 2019; Liu, Liu, Tabuchi, & Wu, 2016; Thomas Papouin, Dunphy, Tolman, Dineley, & Haydon, 2017; Tomita, Ueno, Mitsuyoshi, Kume, & Kume, 2015) and kidney disease (Wiriyasermkul et al., 2020). Despite the significance of D-serine in critical physiological and pathophysiological processes, aspects of the D-serine signalling pathway remain elusive. While it is thought that D-serine is a gliotransmitter released from astrocytes (Henneberger et al., 2010; Thomas Papouin, Henneberger, Rusakov, & Oliet, 2017; Yang et al., 2003), its cellular origin continues to be an intensely debated topic (Thomas Papouin, Henneberger, et al., 2017; Herman Wolosker, Balu, & Coyle, 2016). Progress towards understanding the D-serine pathway has been partly hindered by the lack of a method to study the transmitter dynamically with high spatial and temporal resolution. While methods such as microdialysis can provide precise quantification of D-serine from tissues (Shippenberg & Thompson, 2001), they tend to suffer from poor temporal resolution and can cause mechanical damage to the tissue under study (Beyene, Yang, & Landry, 2019; Ganesana, Lee, Wang, & Venton, 2017). Amperometric probes for D-serine based on DAAO have also been developed by several groups (Mohd Zain, Ab Ghani, & O'Neill, 2012; Pernot et al., 2008); however, these probes are subject to losses in sensitivity due to fouling of the outer biolayer and loss of enzymatic activity during operation (Dale, Hatz, Tian, & Llaudet, 2005), and also have a low spatial resolution.

Optical biosensors are an alternative to existing D-serine detection methods that have the potential to provide unparalleled spatial and temporal resolution when used with high resolution microscopy. Those based on Förster resonance energy transfer (FRET) are commonly a fusion of a ligand-binding domain to a pair of donor-acceptor fluorophores. Here, ligand-induced conformational changes in the binding domain lead to the displacement of the fluorophores and a measurable

change in FRET efficiency (Kaczmarski, Mitchell, Spence, Vongsouthi, & Jackson, 2019). Several FRET-based biosensors of this architecture have been engineered for the dynamic study of key amino acids in brain tissue, including L-glutamate (Okumoto et al., 2005), glycine (Zhang et al., 2018), and L-arginine (Whitfield et al., 2015). The development of such a sensor for D-serine has previously been limited, because no appropriate D-serine-specific solute-binding protein (SBP) is known.

The limitations of naturally occurring SBPs on biosensor design can be overcome by using protein engineering to modify existing SBPs towards desirable binding affinity and specificity. In the case of promiscuous SBPs, however, engineering for both strength and preference of a chosen on-target interaction can be challenging. While improvements in affinity alone can be driven by non-specific hydrophobic interactions, modifying specificity generally requires finer tuning of the charge and shape complementarity between the binding interface and the target ligand. This has been demonstrated in previous work where a SBP (Atu2422) that promiscuously bound glycine, L-serine and GABA, was engineered towards glycine-specificity through multiple rounds of computational design and experimental testing (Zhang et al., 2018). Also highlighted in this work was the challenge of achieving specificity in SBPs that promiscuously bind multiple, structurally similar ligands, requiring a combination of both positive and negative selection.

In this study, we used rational and computational protein design to engineer a D-serine FRET sensor (D-SerFS), using a D-alanine binding protein from *Salmonella enterica* (DalS) (Osborne et al., 2012) as a starting point. Iterative rounds of design and experimental testing produced a robust, D-serine-specific fluorescent sensor with high affinity for D-serine ($K_D$ = 7 – 9 μM). *In-situ* testing of D-SerFS in acute hippocampal rat brain slices demonstrated a response (DR = 6.5%) to exogenously applied D-serine. Furthermore, we demonstrate that D-SerFS responds to extracellular changes of D-serine in the living animal.

## Results

**Homology-guided design of a D-serine-specific binding protein.** A SBP from *Salmonella enterica*, DalS, that binds D-alanine and glycine (Osborne et al., 2012) was chosen as a starting point for the design of a D-serine-specific binding protein. The initial design was guided by a comparison to the NR1 binding domain of the NMDAR, a structural homologue of SBPs that contains the receptor's D-serine/glycine-binding site (Furukawa & Gouaux, 2003). A structural alignment of DalS (PDB 4DZ1) and NR1 (PDB 1PB8) (Fig. **1A**) revealed key differences in the polarity and cavity-size of the two binding sites, particularly at the residues comprising the D-alanine methyl side chain pocket, F117, A147 and Y148 (*vs.* L146, S180 and V181 in NR1). Thus, these residues were targeted for mutagenesis towards D-serine specificity in DalS.

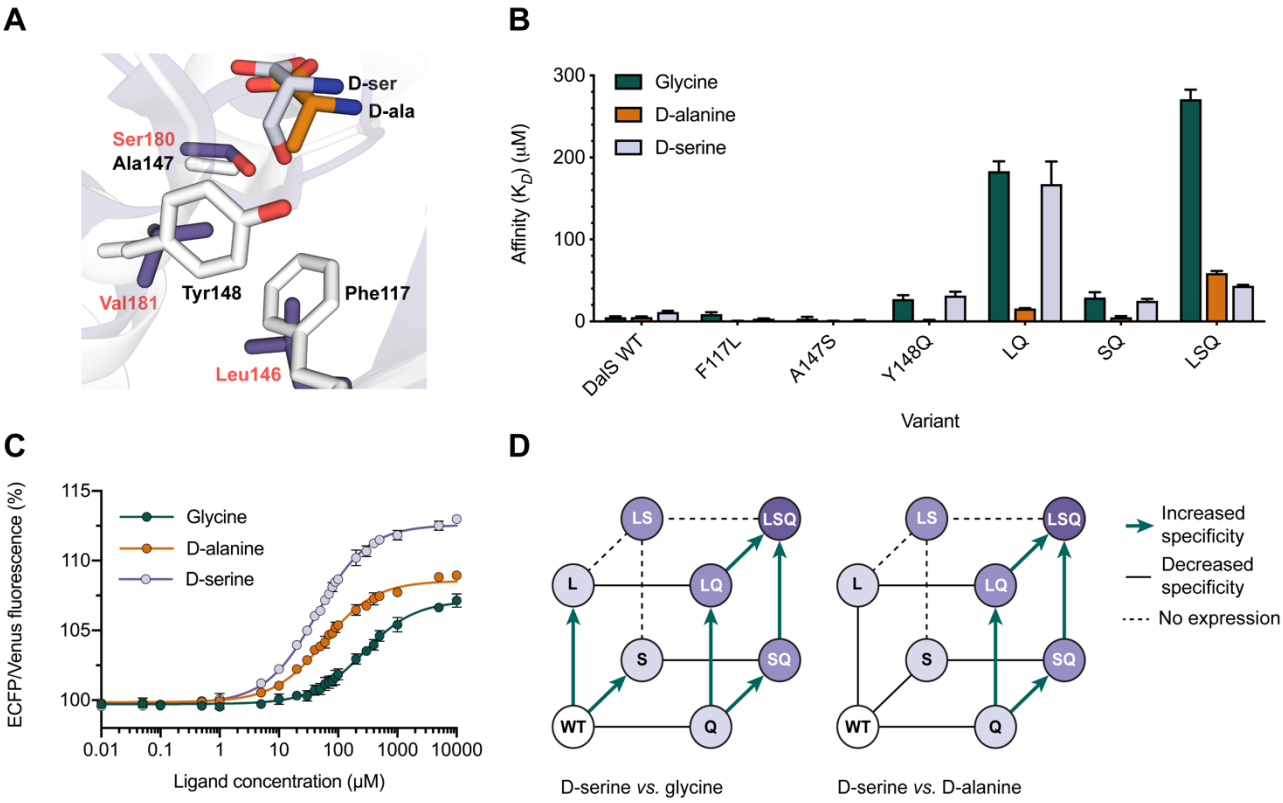


***Figure 1.*** *Homology-guided design of DalS. A) Structural alignment of binding site residues targeted for mutagenesis in DalS (white, black labels; PDB 4DZ1) to homologous residues in the NR1 binding domain (purple, red labels; PDB 1PB8). B) Binding affinities (μM) determined by fluorescence titration of wild-type DalS, and single, double and triple mutants, for glycine, D-alanine and D-serine (n = 3). C) Sigmoidal dose response curves for F117L/A147S/Y148Q (LSQ) with glycine, D-alanine and D-serine (n = 3). Values are the (475 nm/530 nm) fluorescence ratio as a percentage of the same ratio for the apo sensor. D) Schematic demonstrating the epistatic interactions between individual mutations contributing to D-serine specificity relative to glycine (left) and D-alanine (right). Increased D-serine specificity is represented by green arrows, whereas loss in specificity is represented by solid black lines. Dashed lines associated with the variant F117L/A147S (LS) represent the absence of experimental data for this variant due to no maturation of the Venus chromophore during expression.*

Three mutations were initially considered: F117L, A147S and Y148Q. F117L was hypothesised to increase the size of the cavity and reduce van der Waals contacts with the methyl side chain of D-alanine, whilst A147S would increase the polarity of the binding site to form polar contacts with the hydroxyl side chain of D-serine. Y148 was mutated to glutamine rather than valine (as in the NR1 binding site) to increase both the polarity and size of the side chain pocket, reducing potentially favourable interactions with D-alanine and glycine.

To experimentally test the proposed design, DalS was first cloned between enhanced cyan fluorescent protein (ECFP) and Venus fluorescent protein (Venus); a commonly used FRET pair (Bajar, Wang, Zhang, Lin, & Chu, 2016). For immobilization, an N-terminal hexahistidine-tagged biotin domain was included in the construct. F117L, A147S and Y148Q were introduced to the wild-type FRET sensor in a combinatorial fashion. Soluble, full-length protein was obtained in high purity for all variants excluding the double mutant, F117L/A147S (LS). The LS mutant did not exhibit maturation of the Venus chromophore during expression, suggesting that the combination of the two mutations was sufficiently destabilising to the binding protein such that folding of the protein and the downstream Venus fluorescent protein were negatively affected.

Fluorescence titrations with D-alanine, glycine and D-serine were performed on the wild-type protein and the successfully purified variants to determine the binding affinities ($K_D$) (Fig. **1B,** Table **1**). The wild-type exhibited similar affinity to D-alanine and glycine (~5 μM) and significant, but lower, affinity to D-serine (12 μM). Among the single mutants, F117L and A147S increased affinity to D-alanine and D-serine by similar amounts, with minimal effect on glycine affinity. The only mutation that had a large effect in isolation was Y148Q, which had the unintended effect of increasing affinity to D-alanine and decreasing affinity ~8-fold to D-serine. In combination with Y148Q, F117L (LQ) decreased D-alanine affinity ~4.5-fold from Y148Q, while only decreasing D-serine affinity 3-fold, however, A147S (SQ), decreased D-alanine affinity ~3-fold, while increasing D-serine affinity ~3.5-fold. The effects of the mutations in the double mutants on glycine *vs.* D-serine were largely identical. Finally, the combination of the three mutations in F117L/A147S/Y148Q (LSQ), generated a variant that was specific for D-serine, exhibiting a $K_D$ for D-serine of 43 ± 1 μM, compared to 59 ± 2 μM and 271 ± 16 μM for D-alanine and glycine, respectively (Fig. **1C**). The 6.3-fold higher affinity for D-serine *vs.* glycine is the more important comparison because of the spatial and temporal overlap between these in the brain; D-alanine, in contrast, is present in concentrations near or below detection levels in brain tissue (Hashimoto et al., 1992; Popiolek, Tierney, Steyn, & DeVivo, 2018). LSQ displayed a dynamic range of 13% in response to a saturating concentration of D-serine. The combinatorial analysis of the effects of these mutations is indicative of strong epistasis, i.e. the effects of the mutations are not additive and there is no smooth pathway of stepwise increases in D-serine specificity available by which we could arrive at the LSQ variant (Fig. **1D**). This strong epistasis highlighted the advantage of adopting a rational design approach to engineering the binding site, allowing for the introduction of all three mutations simultaneously, even though there were few encouraging signs in the affinities of the single and double mutants.

**Table 1**. Summary of the binding affinities for D-alanine, glycine and D-serine (μM), specificities and thermostabilities (°C) for all variants of the wild-type sensor. D-serine specificity of the variants relative to glycine ($\alpha_{Gly}$) and D-alanine ($\alpha_{D\text{-}ala}$) is defined as the ratio between the $K_D$ for D-serine and that of the corresponding off-target ligand: $\frac{K_d\ for\ Glycine\ (or\ D-alanine)}{K_d\ for\ D-serine}$. Values are mean ± s.e.m. throughout (n = 3).

| Variant | Binding Affinity, $K_D$ (μM) | | | Specificity | | Tm (°C) |
|---|---|---|---|---|---|---|
| | D-ala | Gly | D-ser | $\alpha_{Gly}$ | $\alpha_{D\text{-}ala}$ | |
| WT | 5.4 ± 0.4 | 5 ± 1 | 12 ± 1 | 0.42 | 0.45 | 68.0 ± 0.3 |
| F117L | 0.65 ± 0.03 | 9 ± 1 | 3.7 ± 0.2 | 2.40 | 0.18 | 63.1 ± 0.3 |
| A147S | 0.62 ± 0.03 | 4.0 ± 0.2 | 1.8 ± 0.4 | 2.22 | 0.34 | 66.9 ± 0.4 |
| Y148Q | 1.6 ± 0.3 | 75 ± 8 | 101 ± 3 | 0.74 | 0.02 | 62.0 ± 0.2 |
| (LS) F117**L**/A147**S**† | - | - | - | - | - | - |
| (LQ) F117**L**/Y148**Q** | 32 ± 2 | 340 ± 14 | 309 ± 19 | 1.10 | 0.10 | 60.3 ± 0.2 |
| (SQ)A147**S**/Y148**Q** | 5.4 ± 0.5 | 29 ± 2 | 28 ± 3 | 1.04 | 0.19 | 60.8 ± 0.2 |
| (LSQ) F117**L**/A147**S**/Y148**Q** | 59 ± 2 | 271 ± 16 | 43 ± 1 | 6.30 | 1.44 | 60.5 ± 0.2 |
| (LSQ+E) LSQ + D216**E** | 118 ± 3 | 429 ± 21 | 41 ± 1 | 10.46 | 2.88 | 62.2 ± 0.2 |
| (LSQE+D) LSQE + A76**D** | 130 ± 4 | 410 ± 100 | 48 ± 4 | 8.54 | 2.71 | 65.0 ± 0.1 |
| (LSQED+K) LSQED + S60**K** | 180 ± 1 | 540 ± 13 | 61.0 ± 0.2 | 8.85 | 2.95 | 66.3 ± 0.1 |
| (LSQED+E) LSQED + S208**E** | 120 ± 3 | 420 ± 93 | 40 ± 1 | 10.50 | 3.00 | 66.2 ± 0.1 |
| (LSQED+K) LSQED + N200**K** | 230 ± 63 | 1400 ± 1000 | 470 ± 270 | 2.98 | 0.49 | 69.4 ± 0.1 |
| (LSQED+D) LSQED + T172**D** | - | - | - | - | - | 71.0 ± 0.7 |
| (LSQED+R) LSQED + S60**R** | 202 ± 42 | 1200 ± 380 | 70 ± 17 | 17.14 | 2.89 | 79.0 ± 0.3 |
| (LSQED+Y) LSQED + T197**Y** | 13 ± 1 | 41 ± 17 | 7.0 ± 0.4 | 5.86 | 1.86 | 79.0 ± 0.3 |
| (LSQED+RY) LSQED + S60**R**/T197**Y** | 14 ± 1 | 49 ± 10 | 6.1 ± 0.5 | 8.03 | 2.30 | * |

† This variant did not yield mature fluorescent protein.

* Indicates that a sigmoidal transition in fluorescence ratio as a function of increasing temperature was not observed within the temperature range of the experiment (20 – 85 °C), suggesting a Tm higher than ~ 85 °C.

**Increasing D-serine specificity of LSQ using ligand docking.** In order to identify mutations to the binding site that would further increase the specificity of LSQ for D-serine, modelling of the LSQ binding protein with FoldX (Schymkowitz et al., 2005) and ligand docking with Glide (Friesner et al., 2004), were performed. As LSQ maintained similar affinities for D-alanine ($K_D$ = 59 ± 2 μM) and D-serine ($K_D$ = 43 ± 1 μM), both ligands were docked into the binding site of a model of LSQ and the top poses were analysed (Fig. **2A**). In agreement with *Osborne et al.* (Osborne et al., 2012), the poses suggested that R102 and S97 stabilise the carboxylate group of all docked ligands. It appears that D216, N115, and Y173F, likely play roles in ligand binding and specificity given their proximity to the side chains. Thus, these residues were rationally mutated *in silico* for subsequent rounds of ligand docking.

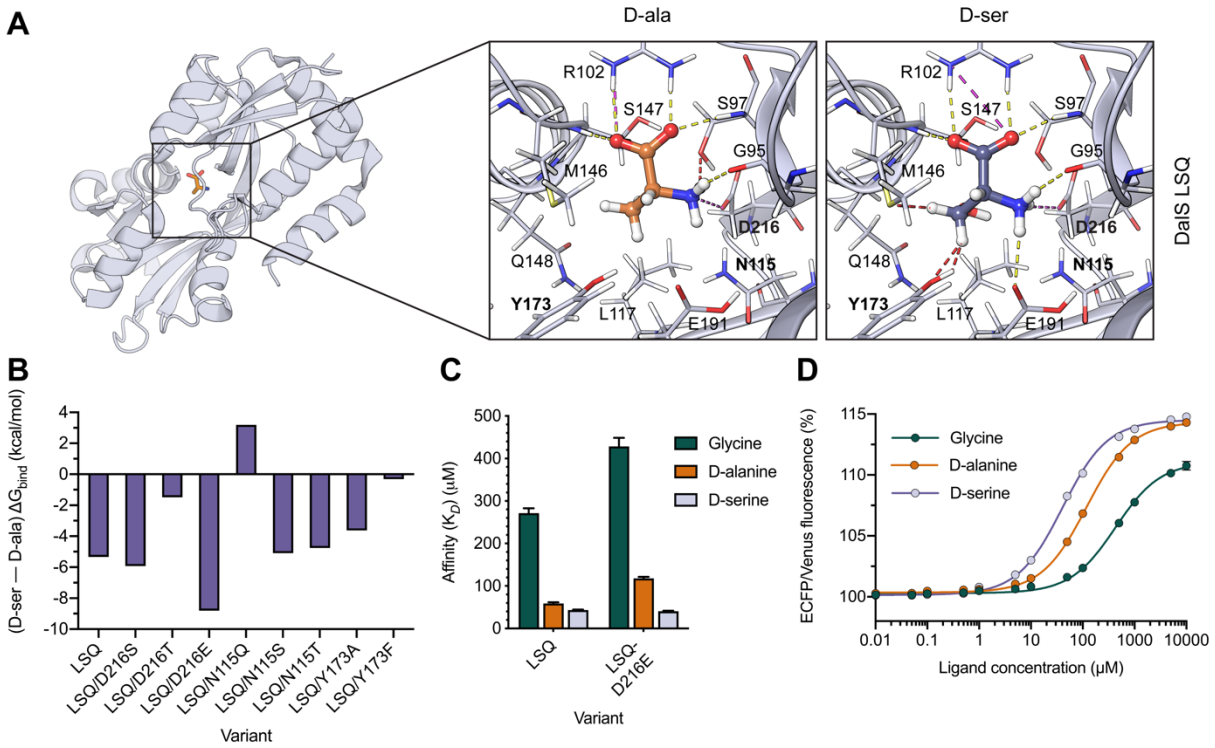


***Figure 2.*** *Ligand docking of the LSQ binding protein using Glide (Friesner et al., 2004). A) Top binding poses of D-alanine (orange, left) and D-serine (purple, right) in a FoldX-generated (Schymkowitz et al., 2005) model of DalS with mutations F117L, A147S, and Y148Q (DalS LSQ). Dashed lines represent non-covalent interactions between binding site residues and the ligands, including hydrogen bonds (yellow), salt-bridges (pink) and unfavourable clashes (red). Residues targeted for further rational design, N115, Y173 and D216, are bolded. B) Difference between* $\Delta G_{bind}$ *(kcal/mol) for D-serine and D-alanine, predicted using Prime MM-GBSA (Rapp, Kalyanaraman, Schiffmiller, Schoenbrun, & Jacobson, 2011) for FoldX-generated models of DalS LSQ and single mutants in the background of DalS LSQ. C) Binding affinities (μM) determined by fluorescence titration of LSQ and LSQ/D216E (LSQE), for glycine, D-alanine and D-serine (n = 3). D) Sigmoidal dose response curves for LSQE with glycine, D-alanine and D-serine (n = 3). Values are the (475 nm/530 nm) fluorescence ratio as a percentage of the same ratio for the apo sensor.*

We first mutated, *in silico*, each residue to the corresponding residue in the NR1 domain, giving rise to LSQ-D216S, -N115Q, and -Y173A. As the carboxylic acid functional group on D216 was predicted to form stabilising interactions with the amine group of both D-alanine and D-serine, the mutation of this residue to glutamate, D216E, was performed. The introduction of other polar residues at positions 115 and 216 was also explored, leading to the mutants LSQ-D216T, -N115T, and -N115S. Lastly, as the side chain of Y173 was predicted to clash with the D-serine ligand in LSQ, the mutation of this residue to phenylalanine, Y173F, was investigated. D-serine and D-alanine were docked into FoldX (Schymkowitz et al., 2005) models of the proposed mutants of LSQ and the generated poses were analysed by visual inspection. In order to quantify and compare the effects of the mutations on binding specificity, Prime MM-GBSA was used to predict the free energy of binding

($\Delta G_{bind}$) in kcal/mol for each ligand. Prime MM-GBSA can effectively predict the relative, rather than absolute, binding free energies for congeneric ligands (Lyne, Lamb, & Saeh, 2006; Rapp et al., 2011). Due to this, focus was placed on the difference between the $\Delta G_{bind}$ for D-serine and D-alanine for each mutant, where positive and negative values corresponded to preferential binding of D-alanine and D-serine, respectively (Fig. **2B**). Using this approach, D216E appeared to be the most beneficial mutation for increasing D-serine specificity ($\Delta G_{bind}$ difference = -8.8 kcal/mol) relative to LSQ ($\Delta G_{bind}$ difference = -5.3 kcal/mol) and was selected for experimental characterisation. The remaining single mutations did not exhibit $\Delta G_{bind}$ differences that were indicative of increased D-serine specificity.

Experimental testing of LSQ/D216E (LSQE) revealed improved specificity towards D-serine. Fluorescence titrations showed that it decreased the affinity of the sensor for both D-alanine ($K_D$ = 118 ± 3 *vs.* 59 ± 2 μM) and glycine ($K_D$ = 429 ± 21 *vs.* 271 ± 16 μM), whilst the affinity for D-serine was slightly increased ($K_D$ = 41 ± 1 *vs.* 43 ± 1 μM) compared to LSQ (Fig. **2C – D**). Furthermore, this improvement in specificity did not affect the dynamic range of the sensor. As a result, LSQE was taken forward for an additional round of engineering.

**Table 2**. Scores computed by Glide (Friesner et al., 2004) and Prime MM-GBSA (Rapp et al., 2011). Glide scores (kcal/mol) and relative binding free energies ($\Delta G_{bind}$) predicted by Prime MM-GBSA for the top poses of D-alanine (D-ala) and D-serine (D-ser) are shown. The difference between the $\Delta G_{bind}$ of D-ser and D-ala represents the predicted specificity of each variant.

| **Variant** | **Glide Score (kcal/mol)** | | **$\Delta G_{bind}$ (kcal/mol)** | | **(D-ser – D-ala) $\Delta G_{bind}$ (kcal/mol)** |
|---|---|---|---|---|---|
| | **D-ala** | **D-ser** | **D-ala** | **D-ser** | |
| WT | -6.6 | -7.4 | -27.9 | -29.1 | -1.2 |
| LSQ | -6.0 | -7.9 | -22.5 | -27.8 | -5.3 |
| D216S | -5.5 | -5.0 | -15.1 | -21.0 | -5.9 |
| D216T | -6.0 | -5.9 | -13.3 | -14.8 | -1.5 |
| D216E | -6.0 | -6.3 | -12.0 | -20.8 | -8.8 |
| N115Q | -6.4 | -8.1 | -28.3 | -25.1 | 3.2 |
| N115S | -7.5 | -8.7 | -25.0 | -30.1 | -5.1 |
| N115T | -7.3 | -8.7 | -23.9 | -28.6 | -4.8 |
| Y173A | -6.1 | -7.5 | -20.1 | -23.7 | -3.6 |
| Y173F | -6.9 | -6.6 | -12.8 | -13.1 | -0.3 |

**Stabilising mutations in LSQE improve the affinity and specificity for D-serine.** Preliminary testing of the LSQ variant under two-photon excitation (2PE) fluorescence microscopy showed a decrease in the dynamic range following the reconstitution of lyophilised sensor (**SI. Fig. 1**). As ECFP/Venus is a common FRET pair successfully used in previous sensors that had not suffered a loss in dynamic range following this process (Whitfield et al., 2015; Zhang et al., 2018), this effect was attributed to the inadequate stability of the binding protein. The thermostability of the sensor

variants was determined by measuring the fluorescence ratio (ECFP/Venus) as a function of increasing temperature (Fig. **3A**). This analysis revealed that all of the variants were less thermostable than the wild-type by up to 8 °C, which we assume is very close to the point at which the protein can no longer fold, as was observed for the F117L/A147S variant. The destabilizing effects of these mutations are consistent with the observation that mutations to active/binding/core sites are more often than not destabilizing (Tokuriki, Stricher, Schymkowitz, Serrano, & Tawfik, 2007).

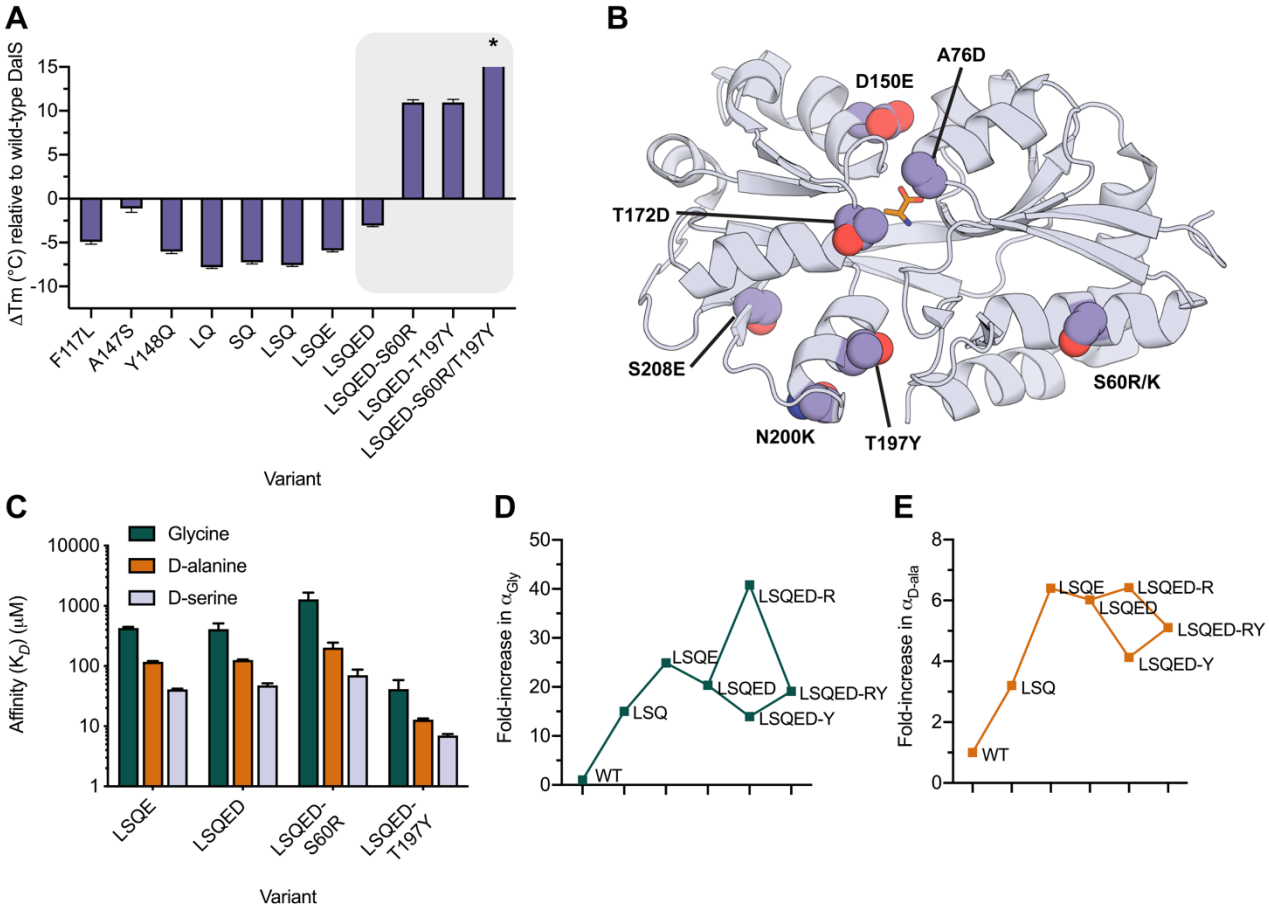


***Figure 3.*** *A) Change in melting temperature of DalS variants relative to the wild-type (ΔTm) (℃). Mutations to the binding site are destabilising. Stabilising mutations to LSQE predicted by FoldX (Schymkowitz et al., 2005) and PROSS (Goldenzweig et al., 2016) are highlighted (grey box). *The ΔTm for LSQED-S60R/T197Y exists outside the axis limit as the unfolding of this variant could not be detected within the temperature range of the experiment (20 – 85 ℃). B) Crystal structure of wild-type DalS (PDB 4DZ1) with the positions of predicted stabilising mutations highlighted (spheres) and labelled. C) Binding affinities (μM) determined by fluorescence titration of LSQE, LSQE-A76D (LSQED), LSQED-S60R (LSQED-R), and LSQED-T197Y (LSQED-Y), for glycine, D-alanine and D-serine. D – E) Fold-increase in D-serine specificity compared to the wild-type for key variants in the design of D-SerFS, relative to glycine (D) and D-alanine (E). Specificity (α) is defined as:* $\frac{K_d \text{ for Glycine (or D-alanine)}}{K_d \text{ for D-serine}}$.

In order to identify potentially stabilising mutations in the binding protein, two computational methods were used: the structure-based FoldX (Schymkowitz et al., 2005) and the sequence and structure-based PROSS (Goldenzweig et al., 2016). Residues on the surface (S60, A76, D150, T172, N200,

S208; Fig. **3B**) were initially targeted for mutation by FoldX as it is known that mutations to the core of a protein are, on average, more destabilizing (Tokuriki et al., 2007). The mutations to each of the other amino acids at each position were ranked by the predicted change in Gibbs free energy of folding (ΔΔG), and the most stabilising mutation at each position that introduced a polar or charged residue to the surface was identified. This produced the following set of mutations: A76D, S208E, S60K, T172D, S60R, N200K, and D150E (Fig. **3B, Table 1**). In parallel, the PROSS webserver developed by Goldenzweig et al. (Goldenzweig et al., 2016) (available at: https://pross.weizmann.ac.il) was also used to identify stabilising mutations. The PROSS algorithm combines phylogenetic analysis and Rosetta-based design to provide users with combinatorial designs predicted to have improved stability relative to the input sequence and structure. A PROSS calculation was performed on the DalS crystal structure and residues with known importance to ligand binding were not allowed to design. This produced the following set of mutations: N32R, S60K, S61A, Q64K, S65E, H67G, L70C, T73V, A76S, G82A, Q88K, E110D, I114T, A123K, H125D, N131D, N133S, N136K, T176A, T176V, T197Y, K199L, L234D, Q242E, S245K, S245Q, G246A, G246E. The individual mutations identified by PROSS were also evaluated with FoldX. All the identified stabilising mutations were then ranked by the ΔΔG values calculated by FoldX (**SI. Table 1**).

Initially, the A76D mutation, which was predicted by FoldX to be the most stabilizing, was selected for experimental testing in the background of the LSQE variant. LSQE/A76D (LSQED) displayed a +3 °C improvement in thermostability (Tm = 65.0 ± 0.1 °C) compared to LSQE and resulted in little change to the binding affinities (Fig. **3C**, **Table 1**). Given this improvement, all mutations with a FoldX ΔΔG that was more negative than 2.5 FoldX standard deviations (< -1.15 kcal/mol) were individually introduced to the background of LSQED. Two variants, LSQED/S208E and LSQED/S60K, displayed no significant improvements (< 1 °C) in thermostability (**Table 1**). The variants, LSQED/T172D and LSQED/N200K exhibited moderate improvements in thermostability (Tm = 71.0 ± 0.7 °C and 69.4 ± 0.1 °C, respectively), while the variants LSQED/S60R (LSQED-R) (Tm = 79.0 ± 0.3 °C) and LSQED/T197Y (LSQED-Y) (79 ± 0.3 °C) resulted in the greatest improvements in thermostability (Fig. **3A**, **Table 1**).

Notably, several of the mutations that were identified to increase thermostability were found to have pronounced effects on substrate affinity and specificity. For example, N200K resulted in a ~10-fold reduction in affinity for D-serine (**Table 1**). In contrast, S60R significantly decreased the affinity for glycine ($K_D$ = 1200 ± 380 μM; Fig **3C**). In a comparison of the fold-change in specificity of key variants relative to the wild-type (Fig. **3D – E**), S60R was found to be the most specific variant, exhibiting a 40-fold and 6-fold greater specificity for D-serine, relative to glycine and D-alanine, respectively, albeit with slightly reduced affinity for D-serine ($K_D$ = 70 ± 17 μM; Fig **3C**). The T197Y mutation was also unexpectedly beneficial for binding and resulted in a marked increase in affinity for D-serine ($K_D$ = 7.0 ± 0.4 μM; Fig. **3C**), as well as for the native ligands D-alanine ($K_D$ = 13 ± 1 μM) and glycine ($K_D$ = 41 ± 17 μM). The T197Y mutant, LSQED-Y, maintained D-serine specificity,

displaying a 14-fold and 4-fold greater specificity for D-serine, relative to glycine and D-alanine, respectively, compared to the wild-type (Fig. **3D – E**). Interestingly, when the mutations S60R and T197Y were included together in the same variant (LSQED-RY), the affinities for D-serine ($K_D$ = 6.1 ± 0.5 μM), D-alanine ($K_D$ = 14 ± 1 μM) and glycine ($K_D$ = 49 ± 10 μM) closely resembled that observed for the T197Y mutation alone (**Table 1**). As no sigmoidal transition in fluorescence ratio as a function of increasing temperature was observed for this variant, this suggested that the thermostability is similar to, or exceeds, the upper limit of the temperature range of the experiment (~ 85 °C; Fig **3A**).

**The molecular basis for the effects of remote mutations on ligand affinity.** The large effect of the T197Y mutation on improving the binding affinities to the three ligands despite being ~13 Å from the binding site was unexpected, prompting further analysis of the molecular basis for this effect. There is no apparent structural explanation for why this remote mutation would change affinity based on the crystal structure of DalS, i.e. there is no mechanism by which it could change the shape of the ligand binding site. Because the crystal structure of DalS is in the ligand bound (closed) conformation, and it is known this protein family fluctuates between open and closed states, we investigated the open-closed conformational transition of the protein scaffold to examine whether the mutation was altering affinity by differentially stabilizing the ligand-bound (closed) state over the unbound (open) state. To do this, we first needed a model of the unbound, open state. Previous work on SBPs closely related to DalS have shown that molecular dynamics (MD) simulations of closed SBP crystal structures in the apo state can reasonably sample open conformational substates (Clifton et al., 2018; Kaczmarski et al., 2020). To simulate the closed to open conformational transition of DalS (PDB 4DZ1), MD simulations (100 ns x 10 replicates) were run with the ligand removed, and clustering analysis was performed to obtain a representative open conformation from the largest cluster. The Cα–Cα distance between residues A85 and K153 (either side of the binding site cleft), and radius of gyration, were calculated for all frames of the simulation (Fig. **4A**). The 85-153 Cα–Cα distance in the open conformation was 0.9 nm greater than that observed in the closed crystal structure (3.0 *vs*. 2.1 nm; Fig **4B**). In the X-ray crystal structures of a closely related SBP, AncCDT-1, the difference in Cα–Cα distance (at equivalent positions) between the open (PDB 5TUJ) and closed (PDB 5T0W) crystallographic states is similar (0.8 nm) (Clifton et al., 2018; Kaczmarski et al., 2020). The difference in the radius of gyration (~1 Å) between the open and closed crystallographic states of AncCDT-1 was also comparable to that observed between the representative open conformation and the closed crystal structure of DalS.

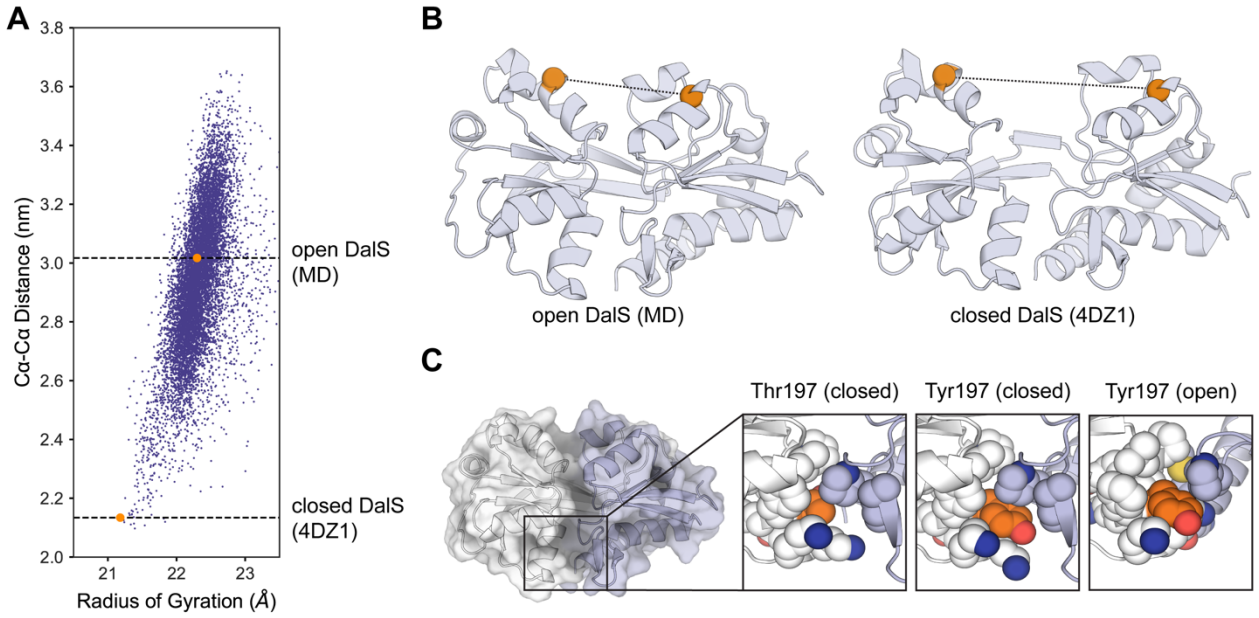


***Figure 4.*** *A) Conformational substates of DalS sampled by MD simulations. The Cα–Cα distance between A85 and K153 is plotted against the radius of gyration where each data point represents a single frame of the MD simulation (sampled every 0.1 ns). Points corresponding to the closed crystal structure of DalS (PDB 4DZ1) and the representative open conformation are highlighted in orange. B) The structure of closed DalS (left) is compared to the structure of the representative open conformation. Residues A85 and K153 are represented by orange spheres, highlighting the difference in Cα–Cα distance. C) Thr197 in the closed crystal structure is compared to FoldX-generated (Schymkowitz et al., 2005) models of the T197Y mutation in the open and closed conformations. Residue 197 (orange spheres) and residues within 4 Å (white spheres) are displayed, showing tighter packing of Tyr197 by surrounding residues in the closed conformation compared to the open conformation. The positioning of Tyr197 at the interface between Lobe 1 (purple) and Lobe 2 (white) is also highlighted.*

T197Y was modelled into the representative open conformation and the closed crystal structure of DalS using FoldX (Schymkowitz et al., 2005). A comparison of Thr and Tyr at position 197 in the closed conformation (Fig. **4C**) showed that the mutation to the larger residue, Tyr, fills a void in the protein between the two lobes and is likely to increase stability by improving hydrophobic packing. Given that residue 197 is positioned at the interface between the two lobes of the binding protein, the improved hydrophobic packing upon mutation to Tyr will stabilise the interaction between them and is likely to stabilize the closed state (relative to Thr). Contrastingly, in the open conformation (Fig. **4C**), Tyr197 is less tightly packed by surrounding residues and is more solvent exposed. This is consistent with the predicted effects on stability as calculated by FoldX, with the calculated ΔΔG for introducing the T197Y mutation to the open and closed conformations being -0.7 and -1.6 kcal/mol, respectively. This was also investigated experimentally: the fluorescence spectra of the LSQED-Y mutant, which displayed a reduced dynamic range *in-vitro* (7%), is consistent with a reduced population of the open state (**SI. Fig. 2**). These results suggest that the remote mutation affects affinity by stabilizing the ligand bound state, which is also consistent with the observation that the affinity increases for all ligands rather than specifically for D-serine (**Table 1**).

**Performance of D-SerFS in hippocampal tissue.** The LSQED-Y variant, which is hereafter referred to as D-SerFS (D-serine FRET Sensor), was selected for *in situ* and *in vivo* testing as a biosensor due to its high D-serine affinity, specificity for D-serine over glycine, and thermostability. Furthermore, additional fluorescence titrations of D-SerFS *in-vitro* confirmed that the sensor did not bind other small molecules prominent in brain tissue (L-serine, GABA, L-glutamate, L-aspartate) with any significance (**SI. Fig. 3**). To test the compatibility of D-SerFS with 2PE fluorescence microscopy, the sensor was imaged at an excitation wavelength of 800 nm in free solution under the objective and titrated with increasing concentrations of D-serine. In these conditions, the sensor exhibited similar affinity and dynamic range to that observed *in vitro* previously (Fig. **5A**), confirming that D-SerFS would be suitable for use with 2PE and thus, within intact tissue. Imaging the sensor over time in a meniscus after applying a saturating concentration of D-serine (10 mM) demonstrated that the ECFP/Venus ratio remained stable over a time course of at least 30 minutes (Fig. **5B**).

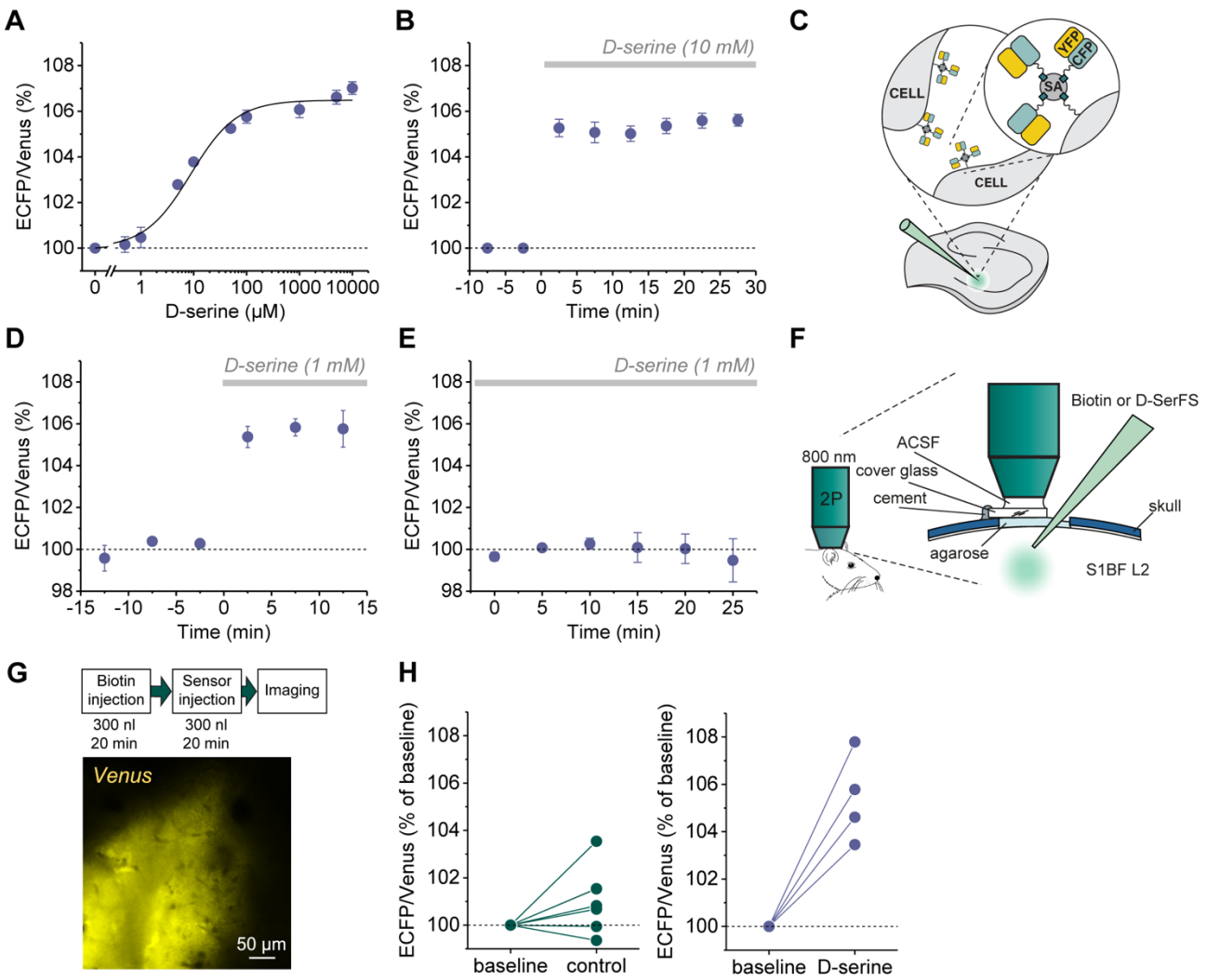


***Figure 5.*** *Characterisation, and in situ and in vivo testing of D-SerFS using 2PE fluorescence microscopy. A) Calibration curve of D-SerFS using 2PE ($\lambda_{exc}$ = 800 nm) shows a dose-dependent change in ECFP/Venus (475 nm/530 nm) ratio. Fitting the relationship between fluorescence ratio and D-serine concentration with a Hill equation obtains a $K_D$ of 8.8 ± 1.6 μM (dynamic range 6.5 ± 0.16 %, n = 3 independent experiments). B) Monitoring of the ECFP/Venus (475 nm/530 nm) ratio in a meniscus after applying 10 mM D-serine demonstrates a stable fluorescence ratio over a time course of 30 minutes (n = 5). C) Illustration of D-SerFS immobilisation in brain tissue. Biotinylated D-SerFS is conjugated to streptavidin (SA) and anchored in the extracellular space of biotinylated slices, as described previously (Whitfield et al., 2015; Zhang et al., 2018). D) Imaging of D-SerFS in response to the exogenous application of 1 mM D-serine in rat brain hippocampal slices (n = 3). E) Monitoring of the ECFP/Venus ratio in rat brain hippocampal slices in the presence of 1 mM D-serine demonstrates a stable fluorescence ratio over a time course of 25 minutes (n = 4). F) Illustration of imaging of D-SerFS in layer two of somatosensory cortex (barrel field, S1BF) in a urethane-anesthetized mouse using 2PE fluorescence microscopy ($\lambda_{exc}$ = 800 nm) G) Schematic of the in vivo testing procedure and image of Venus fluorescence following pressure-loading of D-SerFS into the brain. H) ECFP/Venus ratio recorded in vivo in control recordings (left panel, baseline recording first, control recording after 10 minutes, n = 6) and during D-serine application (right panel, baseline recording first, second recording after D-serine injection, 1 mM, n = 4). Values are mean ± s.e.m. throughout.*

Next, D-SerFS was tested in 350 μm thick acute slices of rat hippocampus. The sensor was anchored in the extracellular space of the CA1 region of biotinylated acute hippocampal slices using

a biotin-streptavidin linker, as described previously (Zhang et al., 2018) (Fig. **5C**). A rapid change in the ECFP/Venus fluorescence ratio was observed following the bath application of 1 mM D-serine to the hippocampal slice (Fig. **5D**). Furthermore, the ratio did not change in the presence of saturating D-serine concentrations for up to 25 minutes (Fig. **5E**), indicating that the indicator is stable in this environment.

The *in vivo* performance of D-SerFS was investigated next. A craniotomy was performed above the barrel field (BF) of the primary somatosensory cortex (S1) of urethane-anaesthetized mice. Twenty minutes after the initial application of biotin, D-SerFS was applied to the same area using a glass micropipette (**Fig. 5F,G,H,** D-serine). The sensor was imaged through the cranial window using 2PE fluorescence microscopy. D-serine (1 mM, 300 nl) was pressure applied to the layer two of somatosensory cortex (130-150 µm depth) using a glass micropipette and the results were compared to control experiments where no D-serine was applied (**Fig 5H**, control). These experiments demonstrate that D-SerFS can be stably immobilized and visualized in the brain of living mice while maintaining its ability to report changes of the ambient D-serine concentrations. They thus pave the way for future experiments visualizing endogenous D-serine signalling.

**Discussion.** In this study, we have constructed the optical sensor D-SerFS and demonstrated its utility in detecting D-serine, an NMDAR co-agonist. In the absence of a suitable D-serine binding protein to use as a recognition domain for the sensor, we used rational and computational design to alter the specificity of an existing D-alanine/glycine binding protein from *Salmonella enterica* (DalS) (Osborne et al., 2012). An initial round of rational design guided by homology to the NR1 binding domain of the NMDAR (Furukawa & Gouaux, 2003), followed by FoldX (Schymkowitz et al., 2005) modelling and Glide (Friesner et al., 2004) ligand docking, led to a variant of DalS (LSQE) that displayed D-serine binding specificity (*vs*. other amino acids). The stepwise introduction of individual binding site mutations towards the proposed rational design demonstrated that there was no single mutational pathway to the improved LSQ variant that displayed improvements at each step owing to the epistatic interactions between these residues. Thus, it was only by introducing all three mutations simultaneously (F117L, A147S, Y148Q) that the improvements to D-serine specificity could be achieved, highlighting the advantage of rational computational design over evolutionary approaches in some instances. Moreover, this allowed us to achieve the improvement in specificity through testing a small number of variants rather than large libraries. However, the affinity of this first round variant (LSQ) for D-serine ($K_D$ = 41 ± 1 µM) was too low to be useful in some biological contexts, such as in neuroscience. Moreover, measurement of the thermostabilities of the mutated variants revealed an overall decrease in thermostability with increased D-serine specificity. As the sensor was required to be robust against the effects of lyophilisation and reconstitution, as well as stable in the crowded environment of brain tissue, we employed the computational methods FoldX (Schymkowitz et al., 2005) and PROSS (Goldenzweig et al., 2016) to identify stabilising mutations to the binding protein. As the mutations predicted by FoldX and the Rosetta-ddG application have

been shown to overlap in only 12 – 25% of all predictions (Buß, Rudat, & Ochsenreither, 2018; Wijma et al., 2014), combining both algorithms had the potential to provide greater coverage of beneficial mutations. In the background of LSQE, the combination of a stabilising surface mutation identified using FoldX (A76D) and a mutation identified using PROSS (T197Y), produced D-SerFS (LSQED-Y), a variant of the sensor that exhibited high thermostability (Tm = 79.0 ± 0.3 °C) and an improved binding affinity for D-serine ($K_D$ = 7.0 ± 0.4 μM), while maintaining specificity for D-serine.

Several stabilising mutations remote from the binding site provided unexpected improvements in binding affinity. In particular, T197Y improved the binding affinity for all ligands while maintaining D-serine specificity. Such effects may be attributed to shifts in the conformational equilibrium of the binding protein. As the binding affinity of a protein for a given ligand may be considered in terms of the equilibria between the open or closed, and apo or bound states, manipulating these equilibria at positions distant from the binding site can lead to changes in affinity, as demonstrated previously (Marvin & Hellinga, 2001). Indeed, investigation of the T197Y mutation in the closed crystal structure of DalS (PDB 4DZ1) and a representative open conformation obtained from MD simulations, suggested that the mutation would stabilize the ligand bound (closed) conformation. The effect of the T197Y mutation on the relative populations of the open and closed conformations is also consistent with the observed decrease in dynamic range (13% in LSQED *vs*. 7% in LSQED-Y). This suggests a possible trade-off between improved binding affinity (*via* stabilisation of the closed conformation) and dynamic range in FRET sensor design. In this instance, the slightly reduced dynamic range caused by the T197Y mutation, was significantly outweighed by the improved thermostability and affinity for D-serine of D-SerFS, which allowed the use of the sensor *in-situ* and *in-vivo*.

Testing D-SerFS in acute hippocampal rat brain slices and in the somatosensory cortex *in vivo* demonstrated that the sensor is responsive to D-serine in the environment of both acute slices and *in vivo* and is compatible with 2PE fluorescence microscopy. D-SerFS displayed similar $K_D$ and dynamic range to that observed *in-vitro*, indicating that stabilisation of the binding protein prevented the loss in dynamic range due to lyophilisation and reconstitution observed in preliminary experiments. Using our calibration data for 2PE in free solution and the maximum fluorescence change to saturating concentration of D-serine in brain tissue (see Zhang et al. 2018 and Whitfield et al. 2015), we can estimate the resting concentration of D-serine to be 1-2 μM. This is in line with previous reports using microdialysis, which also measured extracellular D-serine concentrations in the low micromolar range *in vivo* (rat striatum ~ 8 μM (Ciriacks & Bowser, 2004), rat frontal cortex ~ 6 μM (Matsui et al., 1995), mouse barrel cortex 4.2 μM (Takata et al., 2011)). Since astrocytic $Ca^{2+}$ signalling is a trigger for D-serine release (Henneberger et al., 2010; Thomas Papouin, Dunphy, et al., 2017; Thomas Papouin, Henneberger, et al., 2017; Takata et al., 2011), our slightly lower estimates could be the result of deeper anaesthesia, which can disrupt astrocytic $Ca^{2+}$ signalling (Thrane et al., 2012). Compared to the reported D-serine resting levels, the apparent $K_D$ of D-SerFS

(7-9 μM depending on method) is ideal to detect both increases and decreases of the ambient D-serine concentrations in physiological settings and disease models.

## Conclusions

In this work, we have used computational protein design to engineer an existing glycine/D-alanine binding protein (DalS) towards D-serine specificity and greater stability for use in a FRET-based biosensor for D-serine (D-SerFS). We demonstrated that D-SerFS can be used to detect changes of extracellular D-serine levels in rat brain tissue, providing a new tool for the *in-situ* and *in-vivo* study of the transmitter. Further work on D-SerFS could involve improvement of the dynamic range of the sensor for further *in-situ* and *in-vivo* experiments. This work highlights the utility of computational design tools in engineering naturally occurring binding proteins towards novel specificities, particularly where low-throughput experimental tests of affinity are required to discern the subtle effects of binding site mutations on specificity.

## Materials and Methods

*DNA cloning and mutagenesis*. The DalS (Osborne et al., 2012) wild-type gene was synthesized (GeneArt) for sensor cloning, codon-optimized for expression in *Escherichia coli*. Sensor constructs were cloned into a vector backbone denoted as 'pDOTS10'. This utilizes a vector system described previously (Okumoto et al., 2005) (Addgene Plasmid #13537), which contains a pRSET backbone with an N-terminal 6xHis tag and the insertion of a biotin tag from the PinPoint™ Xa-1 Vector (Promega, USA) in between the His tag and the first fluorescent protein. Endogenous *SapI* sites were removed from the ECFP-Venus cassette, and the binding protein gene YbeJ was replaced with a *SapI* linker (ATCAgaagagcactgcatggtGCGGCCGCcaccactctcgctcttcCCTC) designed around the method of Golden Gate cloning (Engler, Kandzia, & Marillonnet, 2008), whereby *SapI* restriction sites (GCTCTTC/GAAGAGC) are used to clone in a gene of interest. Reciprocal *SapI* sites were added to the 5' and 3' ends of the DalS gene by PCR for subsequent cloning into pDOTS10. Mutations were introduced using a combination of long mutagenesis primers and T7 promoter/terminator primers to create gene fragments with >40 base pair overlaps assembled *via* Gibson Assembly (Gibson et al., 2009). These variants were cloned into a new vector backbone (pETMCSIII), retaining the fluorescent proteins and biotin tag.

*Protein expression and purification*. All proteins were expressed through transformation into BL21(DE3) *E. coli* cells and grown for 72 – 96 h at 18 °C in 1 L autoinducing medium (yeast extract, 5g; tryptone, 20g; NaCl, 5g; $KH_2PO_4$, 3g; $Na_2HPO_4$, 6g in 1 L of water to which 10 ml autoclaved 60% (v/v) glycerol, 5 ml autoclaved 10% (w/v) glucose, 25 ml autoclaved 8% (w/v) lactose were added) supplemented with 100 mg ampicillin. The full expression of the fluorescent protein constructs needed to be monitored by observing the ECFP/Venus spectra over time, with Venus emission typically peaking at 72 h of expression at 18 °C.

Cells were harvested through centrifugation and the pellet was stored at -20 °C prior to purification. For purification, the pellet (frozen or otherwise) was suspended in buffer A (50 mM phosphate, 300 mM NaCl, 20 mM imidazole, pH 7.5), lysed by sonication, re-centrifuged at high speed (13,500 r.p.m. for 45 min at 4 °C) and the clarified supernatant was collected. The supernatant was loaded onto a 5 mL Ni-NTA/His-trap column pre-equilibrated in buffer A, washed with 10 column volumes of buffer A, 5 column volumes of 10% buffer B, and eluted with 100% buffer B (50 mM phosphate, 300 mM NaCl, 250 mM imidazole, pH 7.5). The eluted protein was dialyzed against 3 exchanges of 4 L of buffer C (20 mM phosphate, 200 mM NaCl, pH 7.5) at 4 °C. The dialyzed protein was further purified using a HiLoad 26/600 Superdex 200 pg SEC column using buffer C.

*Fluorescence assays*. Fluorescence titrations were performed on a Varian Cary Eclipse using a Quartz narrow volume fluorescence cuvette. Samples underwent excitation at 433 nm and were scanned over a range of 450 nm – 570 nm for full spectra analysis. ECFP/Venus ratios were

determined using peak wavelength values of 475 nm (ECFP) and 530 nm (Venus). Temperature dependent measurements were obtained using an Applied Photophysics Chirascan™ fluorescence photomultiplier with 433/3 nm excitation and peak fluorescence measured at 475 nm and 530 nm. $K_D$ values were determined by fitting curves with the following equation:

$$y = (y_{min} + \frac{[ligand] * (y_{max} - y_{min})}{(EC_{50} + [ligand])}$$

*Computational assessment of mutations*. Mutations were assessed by first creating the mutation using the BuildModel command in FoldX (Schymkowitz et al., 2005), using the DalS crystal structure (Osborne et al., 2012) (PDB 4DZ1) that had undergone the FoldX Repair process and had the bound ligand removed. Prior to Schrödinger Glide (Friesner et al., 2004) docking, the Protein Preparation Wizard (Madhavi Sastry, Adzhigirey, Day, Annabhimoju, & Sherman, 2013) was used to assign bond orders, generate protonation states and optimize the hydrogen bonding network at pH 7.4. Minimization of the complex using the OPLS3e (Roos et al., 2019) force field was completed with heavy atoms restrained to 0.30 Å of the input structure. Ligands were downloaded in SDF format and LigPrep was used to generate possible ionization states of the ligand at pH 7.4 ± 2.0. In Receptor Grid Generation, the default scaling factor of the Van der Waals radii of receptor atoms (1.0) and partial charge cut-off (0.25) were used. Rotatable receptor hydroxyl and thiol groups were allowed to rotate. The default scaling factor of the Van der Waals radii for the ligand (0.80) and partial charge cut-off (0.15) were used. In Glide, the standard precision (SP) docking method was used with ligand sampling set to the flexible setting, the option of adding Epik state penalties to the docking score included, and post-docking minimization performed. For Prime MM-GBSA (Rapp et al., 2011) calculations, the VSGB solvent model and OPLS3e force field were used in the computation of binding free energy. No residues were allowed to flex during minimization. For the identification of stabilising mutations using FoldX (Schymkowitz et al., 2005), the PositionScan command was used to mutate the targeted positions to each of the other amino acids, using the DalS crystal structure that had undergone the FoldX Repair process and had the bound ligand removed as the input.

*Molecular dynamics simulations and analysis.* The crystal structure of DalS (Osborne et al., 2012) (PDB 4DZ1) was prepared for MD simulation by first building in missing residues using the mutagenesis wizard in PyMOL ("The PyMOL Molecular Graphics System, Version 2.3 Schrödinger, LLC,")and removing the D-alanine ligand. The repaired structure was then capped with an N-terminal acetyl group and C-terminal N-methyl amide group. The protein was solvated in a rhombic dodecahedral box with 13 634 TIP3P water molecules, 37 sodium ions and 41 chloride ions (200 mM salt solution). Simulations were performed using GROMACS version 2018.3 (Abraham et al., 2015) using the CHARMM36m forcefield (Best et al., 2012). Long-range electrostatics were treated with the Particle Mesh Ewald method and the Van der Waals cut-off was set to 1.2 nm. The

temperature was coupled to a virtual water bath at 300 K with a Bussi-Donadio-Parrinello thermostat. The Berendsen barostat was used during equilibrations with a time constant of 2 fs. Production runs were pressure coupled with a Parrinello-Rahman barostat with a time constant of 10 fs. A 2 fs time step was used throughout. Simulations were initially equilibrated with a 2 ns (1 000 000 steps) simulation and production runs were performed for 100 ns each (50 000 000 steps). 10 replicates of the equilibration and production simulations were performed. $C\alpha$–$C\alpha$ distances and radius of gyration for each frame (sampled every 0.1 ns) was calculated using the ProDy package (Bakan, Meireles, & Bahar, 2011). All replicates were concatenated prior to clustering analysis. Clustering was performed using the gromos method for clustering with an RMSD cut-off of 0.2 nm. The middle structure for the largest cluster was taken as the representative open conformation.

*Two-photon excitation (2PE) sensor imaging.* Experiments were performed as previously described (Whitfield et al., 2015; Zhang et al., 2018) with minor changes. We used a FV10MP imaging system (Olympus) optically linked to a femtosecond pulse laser (Vision S, Coherent) equipped with a 25x (NA 1.05) objective (Olympus). See below for in vivo imaging. For titrations in solution, D-SerFS was imaged in a meniscus of PBS at a laser power of 3 mW and increasing amounts of D-SerFS (in PBS) were added. For slice experiments (see below for further details), the laser power was adjusted for depth in the tissue to obtain, on average, a fluorescence intensity corresponding to that of 2-3 mW laser power at the slice surface. The excitation wavelength was 800 nm throughout. Fluorescence of ECFP and Venus fluorescent protein was separated using appropriate band pass filters and dichroic mirrors and detected with photomultiplier tubes connected to a single photon counting board (Picoharp, Picoquant). Their arrival times were recorded using Symphotime 1.5 software (Picoquant). Offline analysis was performed using OriginPro 2017 (OriginLab) and custom written scripts in Matlab R2017a (Mathworks). The ratio of ECFP and Venus fluorescence (R) was calculated from the number of photons detected by the respective detectors in time bins of ~ 220 ms. The photon count rate 11.5 ns to 12.5 ns after the laser pulse (81-82 MHz repetition rate) was subtracted to reduce the contribution of photons not originating from D-SerFS to analysis.

*Brain slice preparation*. Acute hippocampal slices were prepared from three- to five-week-old male Wistar rats as previously described (Anders et al., 2014; Zhang et al., 2018). All animals used in this study were housed under 12 h light/dark conditions and were allowed ad libitum access to food and water. Briefly, 350 µm thick horizontal slices containing hippocampal formation were obtained in full compliance with national and institutional regulations (Landesamt für Natur, Umwelt und Verbraucherschutz Nordrhein-Westfalen and University of Bonn Medical School) and guidelines of the European Union on animal experimentation. Slices were prepared in an ice-cold slicing solution containing (in mM): NaCl 60, sucrose 105, KCl 2.5, $MgCl_2$ 7, $NaH_2PO_4$ 1.25, ascorbic acid 1.3, sodium pyruvate 3, $NaHCO_3$ 26, $CaCl_2$ 0.5, and glucose 10 (osmolarity 305–310 mOsm) and kept in the slicing solution at 34 °C for 15 min before being stored at room temperature in an extracellular

solution containing (in mM) NaCl 131, KCl 2.5, $MgSO_4$ 1.3, $NaH_2PO_4$ 1.25, $NaHCO_3$ 21, $CaCl_2$ 2, and glucose 10 (osmolarity 297–303 mOsm, pH adjusted to 7.4). This solution was also used for recordings. Slices were allowed to rest for at least 50 min. All solutions were continuously bubbled with 95% $O_2$/ 5% $CO_2$.

*D-SerFS imaging in acute slices.* D-SerFS was handled and immobilized in acute hippocampal slices as described before (Whitfield et al., 2015; Zhang et al., 2018). For long-term storage and transport D-SerFS was lyophilized and stored for up to 2 months at ambient temperature (for shipping) and 4° C (storage until use). Before experiments, the sensor was reconstituted in water, agitated for 30 min at room temperature before the buffer was changed to PBS (pH 7.4) with a PD-10 desalting column (GE Healthcare). D-SerFS was then concentrated to 60-100 μM using centricons (Vivaspin 500, 10 kDa cutoff, Sartorius Stedim Biotech). For anchoring of optical sensors in brain tissue, cell surfaces within acute slices were biotinylated using a previously published procedure (Whitfield et al., 2015; Zhang et al., 2018). Briefly, the slice storage solution was supplemented with 50 μM Sulfo-NHS EZ Link Biotin (Thermo Fisher) for 45 min before washing and further storage. Slices were transferred to a submersion-type recording chamber and superfused with extracellular solution at 34 °C. For injections of D-SerFS into the tissue, patch clamp pipettes (2-4 MΩ when filled with PBS saline) were backfilled with PBS (pH 7.4) to which 50-85 μM D-SerFS and 6-10 μM streptavidin (Life Technologies) had been added. The pipette was inserted ~70 μm deep into the tissue under visual control and D-SerFS was pressure-injected. D-SerFS-injected acute slices were allowed to recover for 10-15 minutes before recordings. To reduce the potential effect of scattering of ECFP and Venus fluorescence, we have performed all imaging experiments at a depth of 50-70 μm below the slice surface. Exogenous D-serine was applied via the bath perfusion (1 mM). The following inhibitors were present throughout these experiments to block excitatory synaptic transmission and action potential firing: TTX (1 μM, Sigma Aldrich), D-APV (50 μM, Abcam) and NBQX (10 μM, Tocris).

*In vivo imaging and analysis.* Imaging was performed in the barrel cortex of 8-12 week old C57BL/6 male and female mice as described previously (Monai et al., 2016; Monai et al., 2019). All experimental protocols were approved by the RIKEN Institutional Animal Care and Use Committee. All efforts were made to minimize the number of animals used and their suffering. Under initial isoflurane inhalation anesthesia (3% for induction, 1.5 % for maintenance), the metal frame was attached to the exposed skull using a dental acrylic (Fuji LUTE BC, GC Corporation, Super Bond C&B, Sunmedical) and the mouse head plate was fixed in the stereotactic apparatus and a small craniotomy (about 2.7 mm diameter, 1.5 mm posterior to bregma and 3.5 mm from the midline) was performed using a dental drill. The skull, but not the dura mater, above the right barrel cortex was carefully removed. The cortex was covered with a 1.5% low-melting agarose and a glass cover slip (2.7 mm in diameter) was placed on top and secured by dental cement leaving a small non-covered window for application of biotin, D-SerFS, and D-serine (**Fig. 5F**).

For recordings, mice were anesthetized with an intraperitoneal urethane injection (1.5 g/kg), head-fixed to a strereotactic stage and placed under a 2PE resonant scanner-based microscope (B-Scope, Thorlabs) equipped with a femtosecond Chameleon Vision 2 laser (Coherent) and an Olympus objective lens (XLPlan N 25X). Animals were kept at a constant temperature of 37° C throughout the surgical procedures and the whole experimental session by placing them on a heating blanket (BWT-100 A, Bio Research Center or TR-200, Fine Science Tools). Then the sensor was immobilized in the barrel field of the primary somatosensory cortex as described elsewhere (Okubo et al., 2010) with minor modifications. First, sulpho-NHS-SS-biotin (about 10 mM in PBS, 300 nl) was injected via a glass micropipette at the depth of about 130-150 µm from dura mater at a rate of 50-100 nl per minute. Second, a mixture of D-SerFS and streptavidin was injected (100 µM in PBS, 300 nl) into the same area 20 min after the biotin injection (**Fig. 5D**). Imaging was then performed 20 min after the sensor injection (800 nm excitation wavelength). In a subset of experiments, D-serine (300 nl, 1 mM) was applied to the same area using a glass micropipette. D-SerFS fluorescence was acquired using frame scanning (ThorImage, 512x512 pixels, frame rate 30 Hz). Data were analyzed offline using FIJI (Schindelin et al., 2012).

*Statistics.* Data are reported as mean ± s.e.m. where *n* is the number of independently performed experiments, unless stated otherwise.

**Acknowledgements**

V.V., and J.A.M. acknowledge financial support from an Australian Government Research Training Program Scholarship. Research was funded by an ARC Discovery Project awarded to CJJ. Research in the Fleishman lab was funded by the European Research Council (815379), the Israel Science Foundation (1844), the Milner Foundation and a charitable donation from Sam Switzer and family. The work was further supported by the Human Frontiers Science Program (HFSP; RGY0084/2012 to C.H. and C.J.J.), the German Academic Exchange Service (DAAD-Go8) Travel Fellowship (to C.H. and C.J.J.), the NRW-Rückkehrerprogramm (C.H.) and German Research Foundation (DFG; SFB1089 B03, SPP1757 HE6949/1, FOR2795 and HE6949/3 to C.H.; SPP1757 young investigator grant to P.U.).

**Contributions**

J.H.W, V.V, J.A.M., O.K., S.J.F., and C.J.J. designed, produced and analysed the sensor. P.U., B.B., L.K., and C.H. performed and analysed all experiments using two-photon excitation in acute brain slices. P.U., H.M., and H.H. performed and analysed all *in-vivo* experiments. C.J.J. and C.H. designed the study. C.J.J. and V.V. wrote the initial manuscript, to which all authors subsequently contributed.

## Author information

These authors contributed equally: Vanessa Vongsouthi, Jason H. Whitfield

## Conflict of interest

The authors declare that they have no conflicts of interest with the contents of this article.

**References**


Abraham, M. J., Murtola, T., Schulz, R., Páll, S., Smith, J. C., Hess, B., & Lindahl, E. (2015). GROMACS: High performance molecular simulations through multi-level parallelism from laptops to supercomputers. *SoftwareX, 1-2*, 19-25. doi: https://doi.org/10.1016/j.softx.2015.06.001

Anders, S., Minge, D., Griemsmann, S., Herde, M. K., Steinhäuser, C., & Henneberger, C. (2014). Spatial properties of astrocyte gap junction coupling in the rat hippocampus. *Philosophical Transactions of the Royal Society B: Biological Sciences, 369*(1654), 20130600. doi: https://doi.org/10.1098/rstb.2013.0600

Bajar, B. T., Wang, E. S., Zhang, S., Lin, M. Z., & Chu, J. (2016). A Guide to Fluorescent Protein FRET Pairs. *Sensors (Basel), 16*(9). doi: https://doi.org/10.3390/s16091488

Bakan, A., Meireles, L. M., & Bahar, I. (2011). ProDy: Protein Dynamics Inferred from Theory and Experiments. *Bioinformatics, 27*(11), 1575-1577. doi: https://doi.org/10.1093/bioinformatics/btr168

Basu, A. C., Tsai, G. E., Ma, C. L., Ehmsen, J. T., Mustafa, A. K., Han, L., . . . Coyle, J. T. (2009). Targeted disruption of serine racemase affects glutamatergic neurotransmission and behavior. *Molecular psychiatry, 14*(7), 719-727. doi: https://doi.org/10.1038/mp.2008.130

Best, R. B., Zhu, X., Shim, J., Lopes, P. E. M., Mittal, J., Feig, M., & MacKerell, A. D. (2012). Optimization of the Additive CHARMM All-Atom Protein Force Field Targeting Improved Sampling of the Backbone ϕ, ψ and Side-Chain χ1 and χ2 Dihedral Angles. *Journal of Chemical Theory and Computation, 8*(9), 3257-3273. doi: https://doi.org/10.1021/ct300400x

Beyene, A. G., Yang, S. J., & Landry, M. P. (2019). Review Article: Tools and trends for probing brain neurochemistry. *Journal of vacuum science & technology. A, Vacuum, surfaces, and films : an official journal of the American Vacuum Society, 37*(4), 040802-040802. doi: https://doi.org/10.1116/1.5051047

Bliss, T. V., & Collingridge, G. L. (1993). A synaptic model of memory: long-term potentiation in the hippocampus. *Nature, 361*(6407), 31-39. doi: https://doi.org/10.1038/361031a0

Bliss, T. V. P., & Cooke, S. F. (2011). Long-term potentiation and long-term depression: a clinical perspective. *Clinics (Sao Paulo, Brazil), 66 Suppl 1*(Suppl 1), 3-17. doi: https://doi.org/10.1590/s1807-59322011001300002

Buß, O., Rudat, J., & Ochsenreither, K. (2018). FoldX as Protein Engineering Tool: Better Than Random Based Approaches? *Computational and Structural Biotechnology Journal, 16*, 25-33. doi: https://doi.org/10.1016/j.csbj.2018.01.002

Ciriacks, C. M., & Bowser, M. T. (2004). Monitoring d-Serine Dynamics in the Rat Brain Using Online Microdialysis-Capillary Electrophoresis. *Analytical Chemistry, 76*(22), 6582-6587. doi: https://doi.org/10.1021/ac0490651

Clifton, B. E., Kaczmarski, J. A., Carr, P. D., Gerth, M. L., Tokuriki, N., & Jackson, C. J. (2018). Evolution of cyclohexadienyl dehydratase from an ancestral solute-binding protein. *Nature Chemical Biology, 14*(6), 542-547. doi: https://doi.org/10.1038/s41589-018-0043-2

Corrigan, J. J. (1969). D-Amino Acids in Animals. *Science, 164*(3876), 142. doi: https://doi.org/10.1126/science.164.3876.142

Dai, X., Zhou, E., Yang, W., Zhang, X., Zhang, W., & Rao, Y. (2019). D-Serine made by serine racemase in Drosophila intestine plays a physiological role in sleep. *Nature Communications, 10*(1), 1986. doi: https://doi.org/10.1038/s41467-019-09544-9

Dale, N., Hatz, S., Tian, F., & Llaudet, E. (2005). Listening to the brain: microelectrode biosensors for neurochemicals. *Trends in Biotechnology, 23*(8), 420-428. doi: https://doi.org/10.1016/j.tibtech.2005.05.010

Engler, C., Kandzia, R., & Marillonnet, S. (2008). A One Pot, One Step, Precision Cloning Method with High Throughput Capability. *PLoS ONE, 3*(11), e3647. doi: https://doi.org/10.1371/journal.pone.0003647

Friesner, R. A., Banks, J. L., Murphy, R. B., Halgren, T. A., Klicic, J. J., Mainz, D. T., . . . Shenkin, P. S. (2004). Glide: A New Approach for Rapid, Accurate Docking and Scoring. 1. Method and Assessment of Docking Accuracy. *Journal of Medicinal Chemistry, 47*(7), 1739-1749. doi: https://doi.org/10.1021/jm0306430

Furukawa, H., & Gouaux, E. (2003). Mechanisms of activation, inhibition and specificity: crystal structures of the NMDA receptor NR1 ligand-binding core. *Embo j, 22*(12), 2873-2885. doi: https://doi.org/10.1093/emboj/cdg303

Ganesana, M., Lee, S. T., Wang, Y., & Venton, B. J. (2017). Analytical Techniques in Neuroscience: Recent Advances in Imaging, Separation, and Electrochemical Methods. *Analytical Chemistry, 89*(1), 314-341. doi: https://doi.org/10.1021/acs.analchem.6b04278

Gibson, D. G., Young, L., Chuang, R.-Y., Venter, J. C., Hutchison, C. A., & Smith, H. O. (2009). Enzymatic assembly of DNA molecules up to several hundred kilobases. *Nature methods, 6*(5), 343-345. doi: https://doi.org/10.1038/nmeth.1318

Goldenzweig, A., Goldsmith, M., Hill, S. E., Gertman, O., Laurino, P., Ashani, Y., . . . Fleishman, S. J. (2016). Automated Structure- and Sequence-Based Design of Proteins for High Bacterial Expression and Stability. *Mol Cell, 63*(2), 337-346. doi: https://doi.org/10.1016/j.molcel.2016.06.012

Hardingham, G. E., & Bading, H. (2010). Synaptic versus extrasynaptic NMDA receptor signalling: implications for neurodegenerative disorders. *Nature Reviews Neuroscience, 11*(10), 682-696. doi: https://doi.org/10.1038/nrn2911

Hashimoto, A., Nishikawa, T., Hayashi, T., Fujii, N., Harada, K., Oka, T., & Takahashi, K. (1992). The presence of free D-serine in rat brain. *FEBS Lett, 296*(1), 33-36. doi: https://doi.org/10.1016/0014-5793(92)80397-y

Henneberger, C., Papouin, T., Oliet, S. H. R., & Rusakov, D. A. (2010). Long-term potentiation depends on release of d-serine from astrocytes. *Nature, 463*(7278), 232-236. doi: https://doi.org/10.1038/nature08673

Kaczmarski, J. A., Mahawaththa, M. C., Feintuch, A., Clifton, B. E., Adams, L. A., Goldfarb, D., . . . Jackson, C. J. (2020). Altered conformational sampling along an evolutionary trajectory changes the catalytic activity of an enzyme. *bioRxiv*, 2020.2002.2003.932491. doi: https://doi.org/10.1101/2020.02.03.932491

Kaczmarski, J. A., Mitchell, J. A., Spence, M. A., Vongsouthi, V., & Jackson, C. J. (2019). Structural and evolutionary approaches to the design and optimization of fluorescence-based small molecule biosensors. *Current Opinion in Structural Biology, 57*, 31-38. doi: https://doi.org/10.1016/j.sbi.2019.01.013

Labrie, V., Fukumura, R., Rastogi, A., Fick, L. J., Wang, W., Boutros, P. C., . . . Roder, J. C. (2009). Serine racemase is associated with schizophrenia susceptibility in humans and in a mouse model. *Hum Mol Genet, 18*(17), 3227-3243. doi: https://doi.org/10.1093/hmg/ddp261

Liu, S., Liu, Q., Tabuchi, M., & Wu, M. N. (2016). Sleep Drive Is Encoded by Neural Plastic Changes in a Dedicated Circuit. *Cell, 165*(6), 1347-1360. doi: https://doi.org/10.1016/j.cell.2016.04.013

Lyne, P. D., Lamb, M. L., & Saeh, J. C. (2006). Accurate Prediction of the Relative Potencies of Members of a Series of Kinase Inhibitors Using Molecular Docking and MM-GBSA Scoring. *Journal of Medicinal Chemistry, 49*(16), 4805-4808. doi: https://doi.org/10.1021/jm060522a

Madeira, C., Lourenco, M. V., Vargas-Lopes, C., Suemoto, C. K., Brandão, C. O., Reis, T., . . . Panizzutti, R. (2015). d-serine levels in Alzheimer's disease: implications for novel biomarker development. *Translational Psychiatry, 5*(5), e561-e561. doi: https://doi.org/10.1038/tp.2015.52

Madhavi Sastry, G., Adzhigirey, M., Day, T., Annabhimoju, R., & Sherman, W. (2013). Protein and ligand preparation: parameters, protocols, and influence on virtual screening enrichments. *J Comput Aided Mol Des, 27*(3), 221-234. doi: https://doi.org/10.1007/s10822-013-9644-8

Marvin, J. S., & Hellinga, H. W. (2001). Manipulation of ligand binding affinity by exploitation of conformational coupling. *Nature Structural Biology, 8*(9), 795-798. doi: https://doi.org/10.1038/nsb0901-795

Matsui, T.-a., Sekiguchi, M., Hashimoto, A., Tomita, U., Nishikawa, T., & Wada, K. (1995). Functional Comparison of d-Serine and Glycine in Rodents: The Effect on Cloned NMDA Receptors and the Extracellular Concentration. *Journal of Neurochemistry, 65*(1), 454-458. doi: https://doi.org/10.1046/j.1471-4159.1995.65010454.x

Mohd Zain, Z., Ab Ghani, S., & O'Neill, R. D. (2012). Amperometric microbiosensor as an alternative tool for investigation of D-serine in brain. *Amino Acids, 43*(5), 1887-1894. doi: https://doi.org/10.1007/s00726-012-1365-0

Monai, H., Ohkura, M., Tanaka, M., Oe, Y., Konno, A., Hirai, H., . . . Hirase, H. (2016). Calcium imaging reveals glial involvement in transcranial direct current stimulation-induced plasticity in mouse brain. *Nature Communications, 7*(1), 11100. doi: https://doi.org/10.1038/ncomms11100

Monai, H., Wang, X., Yahagi, K., Lou, N., Mestre, H., Xu, Q., . . . Hirase, H. (2019). Adrenergic receptor antagonism induces neuroprotection and facilitates recovery from acute ischemic stroke.

*Proceedings of the National Academy of Sciences, 116*(22), 11010. doi: https://doi.org/10.1073/pnas.1817347116

Mothet, J.-P., Parent, A. T., Wolosker, H., Brady, R. O., Linden, D. J., Ferris, C. D., . . . Snyder, S. H. (2000). D-Serine is an endogenous ligand for the glycine site of the *N*-methyl-D-aspartate receptor. *Proceedings of the National Academy of Sciences, 97*(9), 4926-4931. doi: https://doi.org/10.1073/pnas.97.9.4926

Okubo, Y., Sekiya, H., Namiki, S., Sakamoto, H., Iinuma, S., Yamasaki, M., . . . Iino, M. (2010). Imaging extrasynaptic glutamate dynamics in the brain. *Proceedings of the National Academy of Sciences, 107*(14), 6526. doi: https://doi.org/10.1073/pnas.0913154107

Okumoto, S., Looger, L. L., Micheva, K. D., Reimer, R. J., Smith, S. J., & Frommer, W. B. (2005). Detection of glutamate release from neurons by genetically encoded surface-displayed FRET nanosensors. *Proc Natl Acad Sci U S A, 102*(24), 8740. doi: https://doi.org/10.1073/pnas.0503274102

Osborne, S. E., Tuinema, B. R., Mok, M. C., Lau, P. S., Bui, N. K., Tomljenovic-Berube, A. M., . . . Coombes, B. K. (2012). Characterization of DalS, an ATP-binding cassette transporter for D-alanine, and its role in pathogenesis in Salmonella enterica. *J Biol Chem, 287*(19), 15242-15250. doi: https://doi.org/10.1074/jbc.M112.348227

Panatier, A., Theodosis, D. T., Mothet, J.-P., Touquet, B., Pollegioni, L., Poulain, D. A., & Oliet, S. H. R. (2006). Glia-Derived d-Serine Controls NMDA Receptor Activity and Synaptic Memory. *Cell, 125*(4), 775-784. doi: https://doi.org/10.1016/j.cell.2006.02.051

Papouin, T., Dunphy, J. M., Tolman, M., Dineley, K. T., & Haydon, P. G. (2017). Septal Cholinergic Neuromodulation Tunes the Astrocyte-Dependent Gating of Hippocampal NMDA Receptors to Wakefulness. *Neuron, 94*(4), 840-854.e847. doi: https://doi.org/10.1016/j.neuron.2017.04.021

Papouin, T., Henneberger, C., Rusakov, D. A., & Oliet, S. H. R. (2017). Astroglial versus Neuronal D-Serine: Fact Checking. *Trends in Neurosciences, 40*(9), 517-520. doi: https://doi.org/10.1016/j.tins.2017.05.007

Papouin, T., Ladepeche, L., Ruel, J., Sacchi, S., Labasque, M., Hanini, M., . . . Oliet, S. H. (2012). Synaptic and extrasynaptic NMDA receptors are gated by different endogenous coagonists. *Cell, 150*(3), 633-646. doi: https://doi.org/10.1016/j.cell.2012.06.029

Pernot, P., Mothet, J.-P., Schuvailo, O., Soldatkin, A., Pollegioni, L., Pilone, M., . . . Marinesco, S. (2008). Characterization of a Yeast d-Amino Acid Oxidase Microbiosensor for d-Serine Detection in the Central Nervous System. *Analytical Chemistry, 80*(5), 1589-1597. doi: https://doi.org/10.1021/ac702230w

Pollegioni, L., & Sacchi, S. (2010). Metabolism of the neuromodulator D-serine. *Cell Mol Life Sci, 67*(14), 2387-2404. doi: https://doi.org/10.1007/s00018-010-0307-9

Popiolek, M., Tierney, B., Steyn, S. J., & DeVivo, M. (2018). Lack of Effect of Sodium Benzoate at Reported Clinical Therapeutic Concentration on d-Alanine Metabolism in Dogs. *ACS Chemical Neuroscience, 9*(11), 2832-2837. doi: https://doi.org/10.1021/acschemneuro.8b00229

The PyMOL Molecular Graphics System, Version 2.3 Schrödinger, LLC.
Rapp, C., Kalyanaraman, C., Schiffmiller, A., Schoenbrun, E. L., & Jacobson, M. P. (2011). A molecular mechanics approach to modeling protein-ligand interactions: relative binding affinities in congeneric series. *Journal of chemical information and modeling, 51*(9), 2082-2089. doi: https://doi.org/10.1021/ci200033n
Roos, K., Wu, C., Damm, W., Reboul, M., Stevenson, J. M., Lu, C., . . . Harder, E. D. (2019). OPLS3e: Extending Force Field Coverage for Drug-Like Small Molecules. *Journal of Chemical Theory and Computation, 15*(3), 1863-1874. doi: https://doi.org/10.1021/acs.jctc.8b01026
Schell, M. J., Molliver, M. E., & Snyder, S. H. (1995). D-serine, an endogenous synaptic modulator: localization to astrocytes and glutamate-stimulated release. *Proceedings of the National Academy of Sciences, 92*(9), 3948-3952. doi: https://doi.org/10.1073/pnas.92.9.3948
Schindelin, J., Arganda-Carreras, I., Frise, E., Kaynig, V., Longair, M., Pietzsch, T., . . . Cardona, A. (2012). Fiji: an open-source platform for biological-image analysis. *Nature methods, 9*(7), 676-682. doi: https://doi.org/10.1038/nmeth.2019
Schymkowitz, J., Borg, J., Stricher, F., Nys, R., Rousseau, F., & Serrano, L. (2005). The FoldX web server: an online force field. *Nucleic Acids Research, 33*(Web Server issue), W382-W388. doi: https://doi.org/10.1093/nar/gki387
Shippenberg, T. S., & Thompson, A. C. (2001). Overview of microdialysis. *Current protocols in neuroscience, Chapter 7*, Unit7.1-Unit7.1. doi: https://doi.org/10.1002/0471142301.ns0701s00
Takata, N., Mishima, T., Hisatsune, C., Nagai, T., Ebisui, E., Mikoshiba, K., & Hirase, H. (2011). Astrocyte Calcium Signaling Transforms Cholinergic Modulation to Cortical Plasticity In Vivo. *The Journal of Neuroscience, 31*(49), 18155-18165. doi: https://doi.org/10.1523/jneurosci.5289-11.2011
Thrane, A. S., Rangroo Thrane, V., Zeppenfeld, D., Lou, N., Xu, Q., Nagelhus, E. A., & Nedergaard, M. (2012). General anesthesia selectively disrupts astrocyte calcium signaling in the awake mouse cortex. *Proceedings of the National Academy of Sciences, 109*(46), 18974-18979. doi: https://doi.org/10.1073/pnas.1209448109
Tokuriki, N., Stricher, F., Schymkowitz, J., Serrano, L., & Tawfik, D. S. (2007). The Stability Effects of Protein Mutations Appear to be Universally Distributed. *J Mol Biol, 369*(5), 1318-1332. doi: https://doi.org/10.1016/j.jmb.2007.03.069
Tomita, J., Ueno, T., Mitsuyoshi, M., Kume, S., & Kume, K. (2015). The NMDA Receptor Promotes Sleep in the Fruit Fly, Drosophila melanogaster. *PLoS ONE, 10*(5), e0128101. doi: https://doi.org/10.1371/journal.pone.0128101
Whitfield, J. H., Zhang, W. H., Herde, M. K., Clifton, B. E., Radziejewski, J., Janovjak, H., . . . Jackson, C. J. (2015). Construction of a robust and sensitive arginine biosensor through ancestral protein reconstruction. *Protein Science, 24*(9), 1412-1422. doi: https://doi.org/10.1002/pro.2721

Wijma, H. J., Floor, R. J., Jekel, P. A., Baker, D., Marrink, S. J., & Janssen, D. B. (2014). Computationally designed libraries for rapid enzyme stabilization. *Protein engineering, design & selection : PEDS, 27*(2), 49-58. doi: https://doi.org/10.1093/protein/gzt061

Wiriyasermkul, P., Moriyama, S., Tanaka, Y., Kongpracha, P., Nakamae, N., Suzuki, M., . . . Nagamori, S. (2020). D-Serine, an emerging biomarker of kidney diseases, is a hidden substrate of sodium-coupled monocarboxylate transporters. *bioRxiv*, 2020.2008.2010.244822. doi: https://doi.org/10.1101/2020.08.10.244822

Wolosker, H., Balu, D. T., & Coyle, J. T. (2016). The Rise and Fall of the d-Serine-Mediated Gliotransmission Hypothesis. *Trends in Neurosciences, 39*(11), 712-721. doi: https://doi.org/10.1016/j.tins.2016.09.007

Wolosker, H., Blackshaw, S., & Snyder, S. H. (1999). Serine racemase: a glial enzyme synthesizing D-serine to regulate glutamate-N-methyl-D-aspartate neurotransmission. *Proc Natl Acad Sci U S A, 96*(23), 13409-13414. doi: https://doi.org/10.1073/pnas.96.23.13409

Yang, Y., Ge, W., Chen, Y., Zhang, Z., Shen, W., Wu, C., . . . Duan, S. (2003). Contribution of astrocytes to hippocampal long-term potentiation through release of D-serine. *Proceedings of the National Academy of Sciences, 100*(25), 15194. doi: https://doi.org/10.1073/pnas.2431073100

Zhang, W. H., Herde, M. K., Mitchell, J. A., Whitfield, J. H., Wulff, A. B., Vongsouthi, V., . . . Henneberger, C. (2018). Monitoring hippocampal glycine with the computationally designed optical sensor GlyFS. *Nature Chemical Biology, 14*(9), 861-869. doi: https://doi.org/10.1038/s41589-018-0108-2